Supporting Information

Non-porous Two-Dimensional Conducting Metal–Organic Frameworks with Enhanced Capacitance Storage

Cheng Chen,[ab] Chongqing Yang,*[c] Xiaobin Fu,[d] Yilong Yang[c], Senhe Huang,[b] Junbo Hou,[e] Min Yang,[f] Yuezeng Su*[a] and Xiaodong Zhuang*[b]

[a.] School of Electronic Information and Electrical Engineering, Shanghai Jiao Tong University, Shanghai 200240, China.

[b.] The meso-Entropy Matter Lab, State Key Laboratory of Metal Matrix Composites, Shanghai Key Laboratory of Electrical Insulation and Thermal Ageing, School of Chemistry and Chemical Engineering, Frontiers Science Center for Transformative Molecules, Shanghai Jiao Tong University, 800 Dongchuan Road, Shanghai 200240, China.

[c.] Carbon Capture and Utilization Research Center, College of Smart Energy, Shanghai Jiao Tong University, Shanghai 200240, China.

[d.] Department of Molten Salt Chemistry and Engineering, Shanghai Institute of Applied Physics, Chinese Academy of Sciences, Shanghai 201800, China.

[e.] Power System Resources Environmental Technology Co. Ltd, 585 Changan north road, Haiyan 314399, China.

[f.] *Shanghai Dianji University, 300 Shuihua Road, Pudong New Area District, Shanghai, 201306.*

Table of Contents

Section I. Experimental Procedures

Materials. Starting materials were purchased from commercial suppliers and were used without further purification unless otherwise noted. Pyrazine (AR, ≥99.5%), tetraethyl orthosilicate (TEOS), ferric chloride (II) (AR, ≥99.5%), chromous chloride (AR, ≥99.5%), dimethyformamide (DMF), acetonitrile (ACN), poly(1,1-difluoroethylene) (PVDF), 1-methyl-2-pyrrolidone (NMP), carbon black and tetraethylammonium tetrafluoroborate (TEABF$_4$) were purchased from Sigma-Aldrich and were used without further purification. All aqueous solutions were prepared with ultrapure water (>18.2 MΩ cm) from a Milli-Q Plus system (Millipore).

Synthesis of FeCl$_2$(pyz)$_2$ (Fe-MOF). 90 ml of 0.5 M pyrazine aqueous solution was added to 10 ml of TEOS, and the mixture was stirred vigorously for 2 hours until the solution became more viscous. The clear solution was then dispersed into five test tubes, covered with parafilm, and allowed to stand until a gel formed. A beaker was filled with ferric chloride (II) and paraffin oil in the Ar-filled glove box. Then 20 ml of 0.5 M ferric chloride (II) solution was prepared by adding 20 ml deoxygenated water to the beaker with a syringe. After thorough mixing, 4 ml of this solution was carefully added to the previously prepared solidified gel. Finally, paraffin oil was added to the top of the solidified gel to prevent exposure to air. After a few days, a single crystal of Fe-MOF was obtained. These crystals were red, square pieces.

Synthesis of CrCl$_2$(pyz)$_2$ (Cr-MOF).[1] 0.2 g of chromous chloride and 2 g of pyrazine ligand were dispersed in a 50 mL hydrothermal reactor. The reaction was then fully reacted in an oven at 200 °C for 24 hours. Subsquently, the product was washed three times with DMF and acetonitrile, and then dried overnight in a vacuum at room temperature to obtain a dark product.

Material Characterization. The X-ray diffraction (XRD) pattern was collected using a Bruker D8 Advance X-ray diffractometer with Cu Kα radiation (λ = 0.15406 nm) at 40 kV and 30 mA at room temperature. Scanning electron microscopy (SEM) and transmission electron microscopy (TEM) images were collected with a field emission scanning electron microscope (FESEM, Zeiss Gemini 500, operating at 3 keV) and a high-resolution transmission electron microscope (HRTEM, JEM-2100, JEOL, Japan), respectively. Mössbauer spectra were recorded with a Topologic 500A spectrometer (Topologic Systems) and a proportional counter at room temperature. FT-IR spectra (KBr) spectra of Fe-MOF were carried out using a 510PFT FT-IR spectrometer. The X-ray photoelectron spectroscopy (XPS) spectra were acquired using a Kratos Axis UltraDLD spectrometer (Kratos Analytical, a Shimadzu Group Company) with a monochromatic Al-Kα source (1486.6 eV). Ultraviolet photoelectron spectroscopy (UPS) measurements were performed in the same chamber with a He I UV source, applying a -5.00 V bias to the sample. Nitrogen physisorption measurements were taken in the relative pressure range of 0.0001–0.9 at 77.3 K using a Micromeritics TriStar II Plus automated, three-station, surface area and porosity analyzer. Raman spectroscopy and mapping were performed on Fe-MOF using a Horiba LabRAM HR Evolution system with a 532 nm excitation laser. Synchrotron X-ray absorption spectroscopy (XAS) data were collected at room temperature in transmission mode at beamline BL14W1 and BL15U1 of the Shanghai Synchrotron Radiation Facility (SSRF, China). The CASTEP program in the Materials Studio package (Accelrys) was used to conduct the DFT calculations.

Electronic property measurements.[2] To measure the electronic properties, the conductivity of Fe/Cr-MOF was determined. The Fe/Cr-MOF powder was pressed into a pellet at a pressure of 1 GPa. The compressed pellet had a thickness of around 0.3 mm and a diameter of 8 mm without any obvious cracks. The various-temperature conductivity was measured in the four-

probe method using a physical property measurement system (PPMS) under high vacuum in the temperature range from 140 to 350 K.

Preparation of the Fe-MOF electrodes. The Fe-MOF electrode slurry was prepared by ultrasonically mixing Fe-MOF powder, carbon black, and poly(1,1-difluoroethylene) (PVDF) in a ratio of 8:1:1 using 1-methyl-2-pyrrolidone (NMP). The slurry was stirred for 30 minutes to form a homogeneous suspension. The well-dispersed active material slurry was then spread on a carbon paper, pressed into a film, and dried overnight in a vacuum oven at 80 ℃. After drying, the film was cut into disks with a diameter of 1.13 cm. The areal loading mass was approximately 0.6 mg cm^{-2}.

Preparation of the Cr-MOF electrodes. The Cr-MOF electrode slurry was prepared by ultrasonically mixing Cr-MOF powder, carbon black, and poly(1,1-difluoroethylene) (PVDF) in a ratio of 8:1:1 with the help of 1-methyl-2-pyrrolidone (NMP). The mixture was stirred for 30 minutes to form a homogeneous suspension. Then the slurry was spread on a carbon paper, pressed into a film, and dried overnight in a vacuum oven. After drying, the film was cut into disks with a diameter of 1.13 cm. The areal loading mass was about 0.6 mg cm^{-2}.

Standard three-electrode system assembly. In a three-electrode system, the Fe/Cr-MOF disk (1.13 cm) was used as the working electrode, platinum wire was acted as the counter electrode, and Ag/AgCl was used as the reference electrode. A solution of 1.0 M TEABF$_4$/acetonitrile was used as the electrolyte. All cells were assembled under dry and oxygen-free conditions in an Ar-filled glove box.

Fabrication of symmetric SCs (Fe- and Cr-MOF//SC). To construct symmetric supercapacitors (SCs), the device had a sandwich-like structure with two Fe/Cr-MOF electrode disks separated by a glass fiber membrane, and then a moderate electrolyte was add in to the cell. All the devices were assembled under dry and oxygen-free conditions in an Ar-filled glove box.

Electrochemical Characterization.[3] All electrochemical measurements, including cyclic voltammetry (CV), galvanostatic charge/discharge (GCD) measurements, and electrochemical impedance spectroscopy (EIS), were performed using a CHI 660E electrochemical workstation at room temperature (25 $^\circ$C). The EIS measurements were carried out from 10 mHz to 100 kHz at bias voltages.

The gravimetric capacitances in the three electrodes were calculated from the GCD profiles according to Equation (1):

$$C_t = I\Delta t/(\Delta V * m) \tag{1}$$

where C_t (F g^{-1}) is the gravimetric capacitance, I /m (A g^{-1}) is the current density, Δt (s) is the discharge time, and ΔV (V) is the potential window.

A full symmetric capacitor can be treated as two capacitors in series. The electrode capacitance values based on the GCD and CV results were calculated according to the Equation (2-5)

$$C_{electrode} = 4\int_{V_t}^{V_i} I(V)\, dV/(2 \times m \times v \times (Vi - Vt)) \tag{2}$$

$$C_{electrode} = 4 \times I\Delta t/(\Delta V * m) \tag{3}$$

$$C_{areal} = C_{electrode} * m/\Delta S \tag{4}$$

$$\frac{1}{C_{cell}} = \frac{1}{C_{electrode}} + \frac{1}{C_{electrode}} \tag{5}$$

where $C_{electrode}$ (F g^{-1}) is denoted as the specific electrode capacitance. I (A) is the charge-discharge current, Δt (s) is the discharge time, ΔV (V) is the voltage change. m (g) is the total mass of active material of the both electrodes. v (mV s^{-1}) is the scan rate. C_{areal} (mF cm^{-2}) is the specific areal capacity. ΔS (cm^{-2}) is the areal of the both electrodes. C_{cell} (F g^{-1}) is the gravimetric capacitance of the cell.

The gravimetric energy density (E, Wh kg^{-1}) and power density (P, kW kg^{-1}) were calculated according to the following Equations (6-7):

$$E = 0.5 \times C_{cell} \times (\Delta V)^2 / 3.6 \tag{6}$$

$$P = E/\Delta t \times 3.6 \tag{7}$$

where C_{cell} (F g^{-1}) is the gravimetric capacitances of the device, ΔV (V) is the voltage window, Δt (s) is the discharge time.

Capacitance contribution calculation method of Trasatti Method.[4] The Trasatti method was used to differentiate between the capacitance contributions from surface and capacitive sources. CV curves of Fe- and Cr-MOF//SCs were collected at scan rates ranging from 6 mV s^{-1} to 50 mV s^{-1}. Plotting the reciprocal of gravimetric capacitance (C^{-1}) against the square root of the scan rate ($\upsilon^{0.5}$). Specifically, the correlation can be described by the following Equation (8):

$$C^{-1} = k\upsilon^{0.5} + C_t^{-1} \tag{8}$$

where C (F g^{-1}) is the experimental gravimetric capacitance, υ (mV s^{-1}) is the scan rate and C_t (F g^{-1}) is the total capacitance. The "total capacitance" is the sum of the EDL capacitance and the pseudo-capacitance.

Plotting the gravimetric capacitances (C) against the reciprocal of square root of scan rates (v$^{-0.5}$). The correlation can be described by the following Equation (9):

$$C = k\upsilon^{-0.5} + C_{capacitive} \tag{9}$$

where C (F g^{-1}) is the experimental gravimetric capacitance, υ (mV s^{-1}) is the scan rate and $C_{capacitive}$ (F g^{-1}) is the maximum capacitive capacitance. Subtraction of $C_{capacitive}$ from C_t yield the surface capacitance.

Electrochemical quartz crystal microbalance (EQCM) method.[5,6] The mass sensitivity of the QCM results from the relationship between the oscillation frequencies, as described by Equation (10):

$$\Delta m = -A\frac{\sqrt{\mu\rho}}{2f^2} \cdot \Delta f = -C_f \cdot \Delta f \tag{10}$$

where the QCM sensor has a fundamental frequency of 7.936984 MHz, A (cm^2) is the area of the active surface (0.196 cm^2), μ (g cm^{-1} s^2) is the shear modulus of quartz (2.947 × 10^{11} g cm^{-1} s^2), and ρ (g cm^{-3}) is the density of the quartz crystal (2.84 g cm^{-3}). The sensitivity factor C$_f$ is 1.42 ng Hz^{-1} cm^{-2}, meaning that 1 Hz change equals 1.42 ng mass change.

The theoretical mass change (Δm) induced by the adsorption/desorption of electrolyte species during cycling can be related to the charge (Q) passing through the electrode using Faraday's law (11):

$$\Delta m = QM/nF \tag{11}$$

where M (g mol^{-1}) is the net molecular weight of the adsorbed electrolyte species, n is the valence of the ions adsorbed/desorbed (for TEA$^+$ and BF4$^-$, n = 1) and F (C mol^{-1}) is the Faraday constant (96485 C mol^{-1}). Therefore, the net molecular weight of the adsorbed/desorbed electrolyte species can be calculated from the slope of the Δm–ΔQ plot using the following Equation (12):

$$M_W/nF = \Delta m/Q \tag{12}$$

From this, the electrolyte species that are adsorbed and desorbed during the electrochemical cycle can be determined.
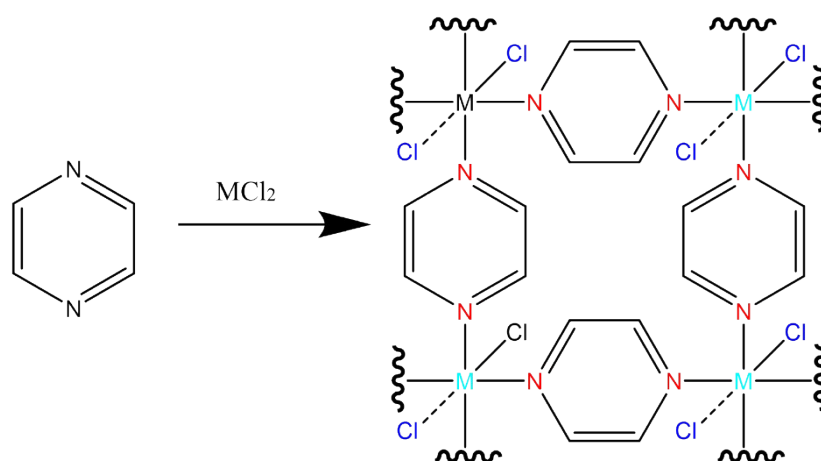
Section Ⅱ. Electrochemical Data

Figure S1. Synthetic route of Fe-MOF and Cr-MOF through the coordination reaction between *pyz* and metal ions (iron and chromium).
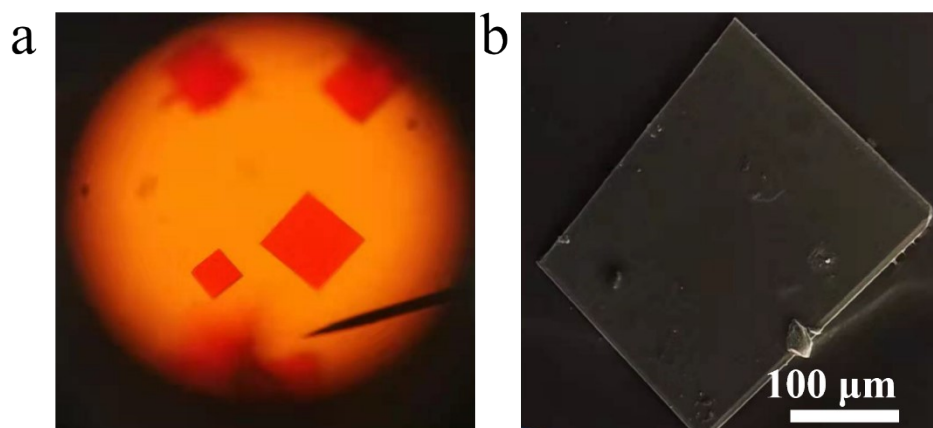
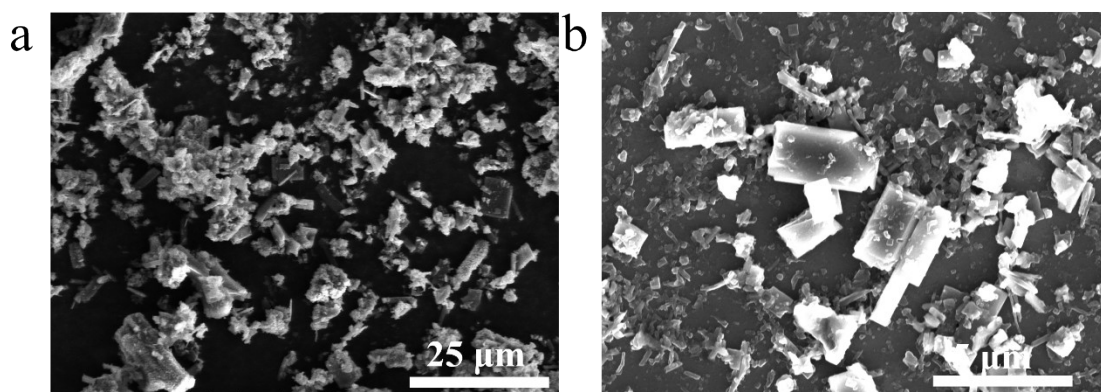**Figure S2.** (a) Optical image and (b) SEM image of Fe-MOF single crystals.

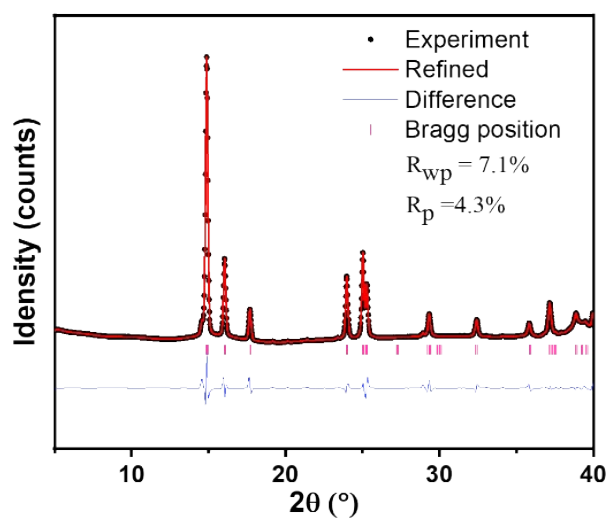**Figure S3.** SEM image of Cr-MOF polycrystals at different magnifications.

Figure 4. Powder X-ray diffraction spectrum (black dots) of Cr-MOF obtained at room temperature. The refined (red line), the difference (blue line) and the calculated line positions (pink bars) are shown.
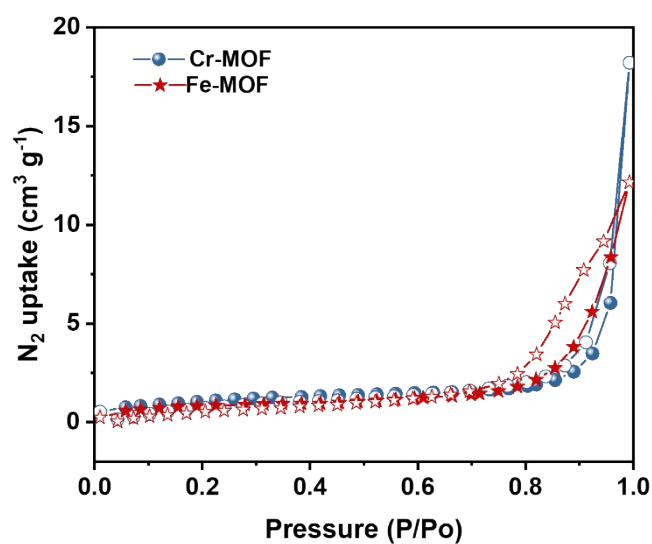
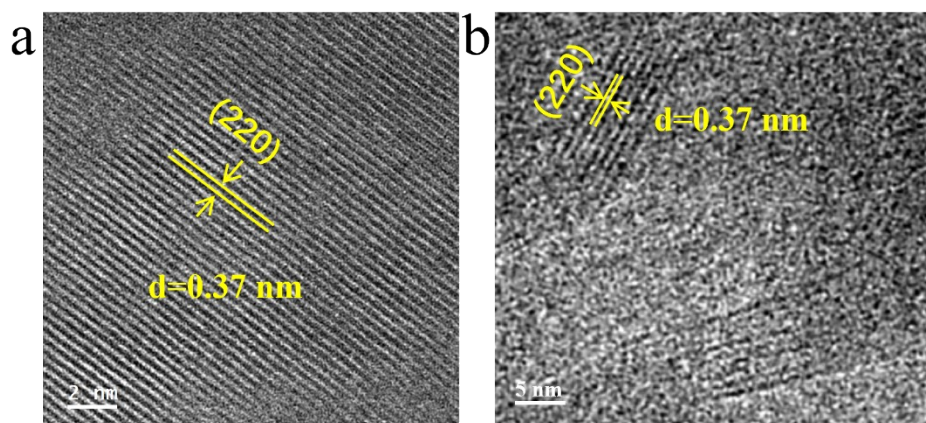**Figure 5.** Nitrogen sorption isotherms of Fe-MOF and Cr-MOF at 77 K.
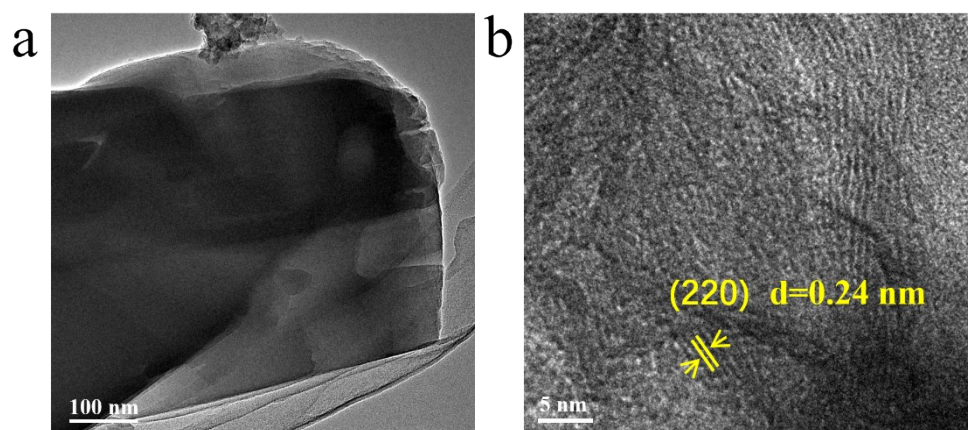
Figure S6. TEM images of Fe-MOF at different magnifications.

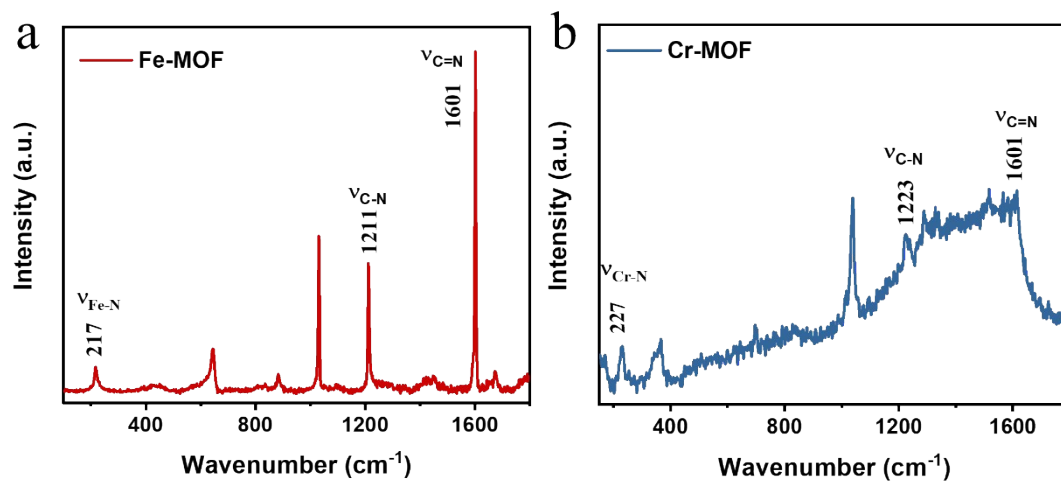

Figure S7. TEM images of Cr-MOF at different magnifications.

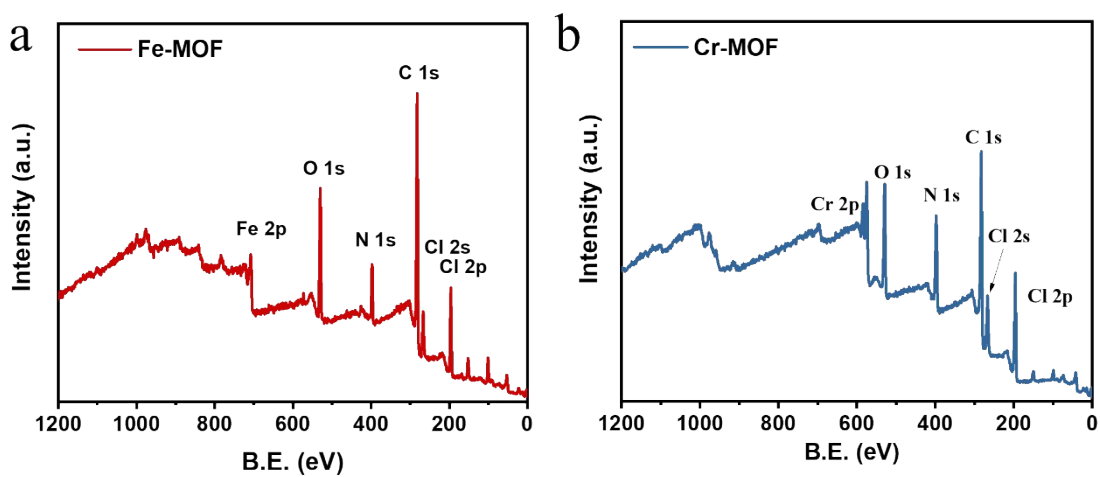**Figure S8.** Raman spectra of Fe-MOF (a) and Cr-MOF (b).
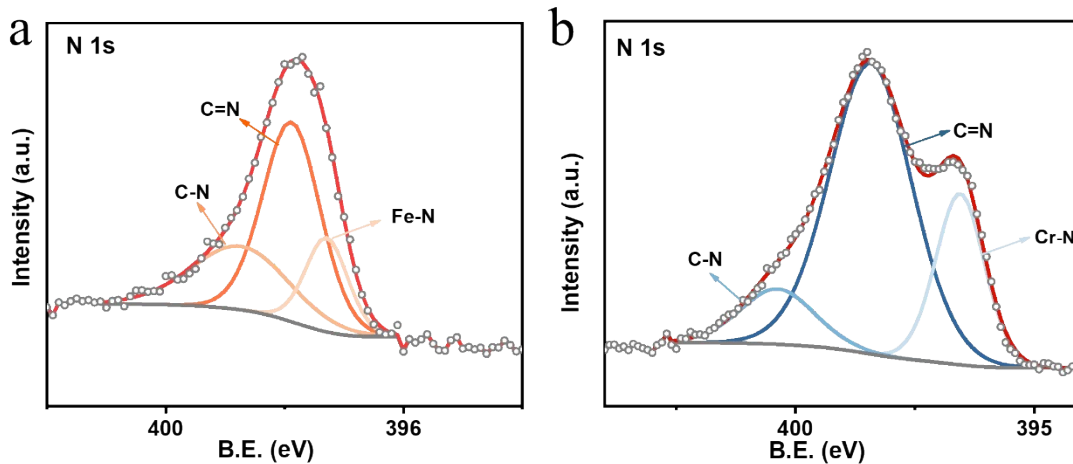

Figure S9. XPS surveis of Fe-MOF (a) and Cr-MOF (b).

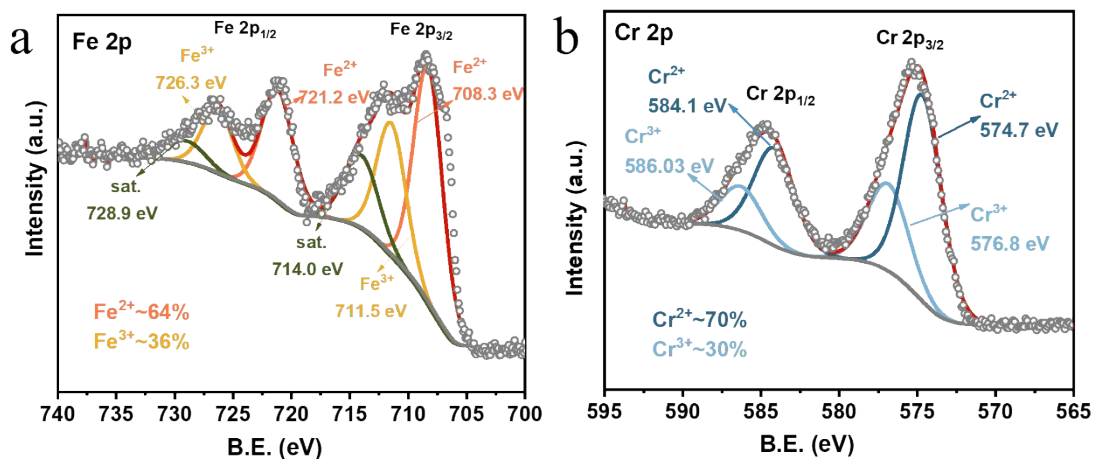**Figure S10.** N 1*s* core level spectra of Fe-MOF (a) and Cr-MOF (b).

Figure S11. (a) Fe 2*p* core-level spectra of Fe-MOF. (b) Cr 2*p* core-level spectra of Cr-MOF.
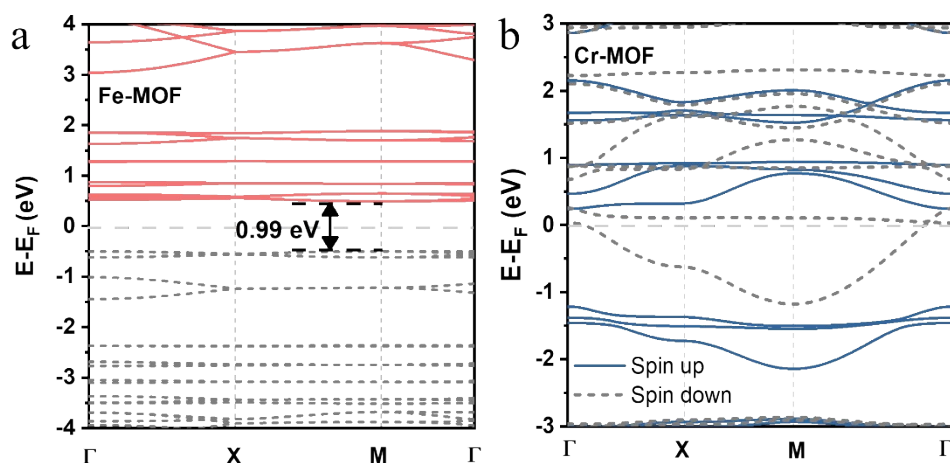
Figure S12. Calculated electronic band structure of a single-layered Fe-MOF (a) and Cr-MOF (b).
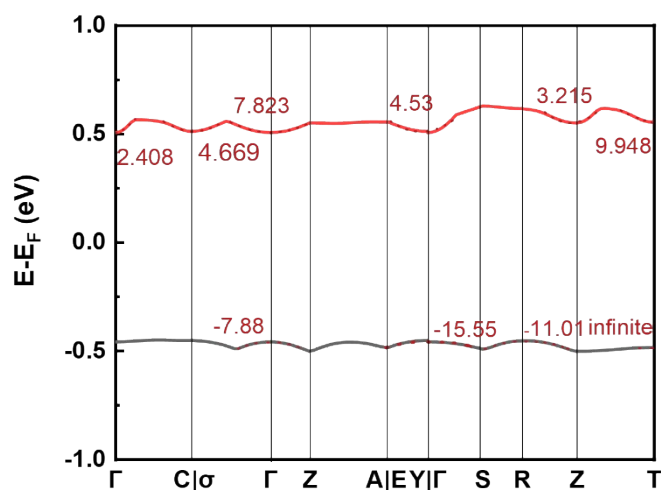

Figure S13. The effective mass of Fe-MOF approximation consists of a quadratic fit to the valence band maximum and conduction band minimum. The curvature gives the effective hole mass (m_h^*) and electron mass (m_e^*).
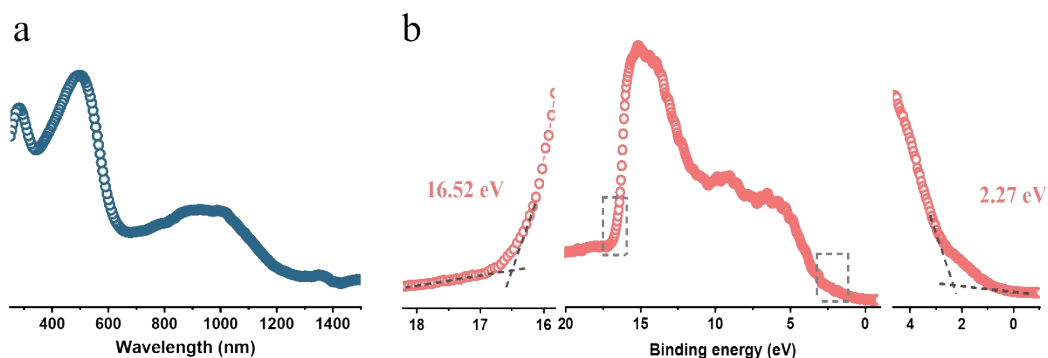
Figure S14. (a) Ultraviolet-visible absorption spectroscopy of Fe-MOF. (b) UPS spectrum of Fe-MOF. The energy level of the HOMO of Fe-MOF was calculated to be approximately 6.75 eV.[7]
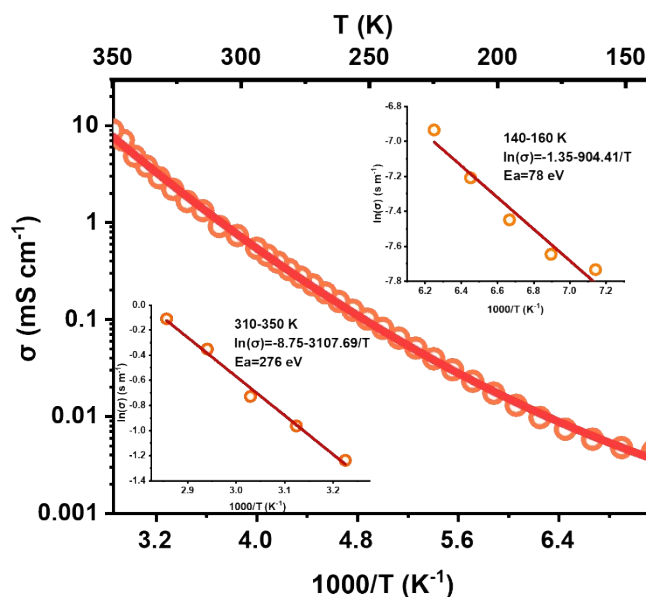
Figure S15. Variable-temperature conductivity of Cr-MOF as a function of inverse temperature. This measurement was performed on a pellet of Cr-MOF by the four-probe method. Inset plots show the activation energy of two different temperature regions.

To describe a thermally activated conduction process, we used a model given in Equation (13):

$$\sigma = \frac{\sigma_1 * T}{exp[E_1/RT]}$$

(13)

where the molecular gas constant R, the preexponential constant σ_1 and the activation energies E_1 are the free parameters. The measured variable-temperature electrical

conductivity data fit to this model quite nicely (from 140 K to 300 K). For Cr-MOF, a high temperature activation region (from 310 to 350 K) with an activation energy of ~276 meV and a low temperature activation region (from 140 to 160 K) with an activation energy of ~78 meV were observed.
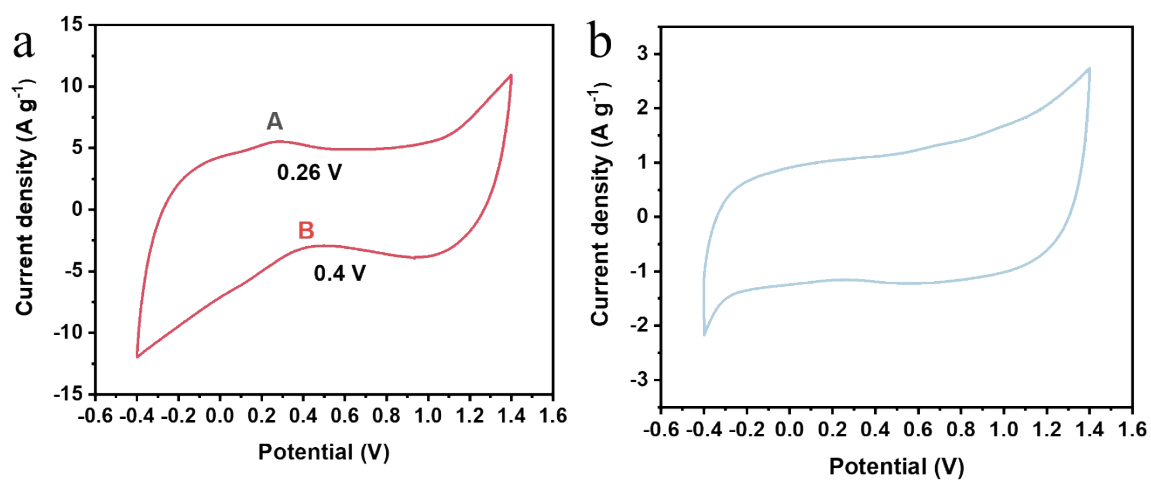
Figure S16. CV curves of the Fe/Cr-MOF electrodes in a three-electrode system at 80 mV s^{-1} in 1 M TEABF$_4$/acetonitrile electrolyte (potential windows: -0.4-1.4 V). (a) Fe-MOF. (b) Cr-MOF.
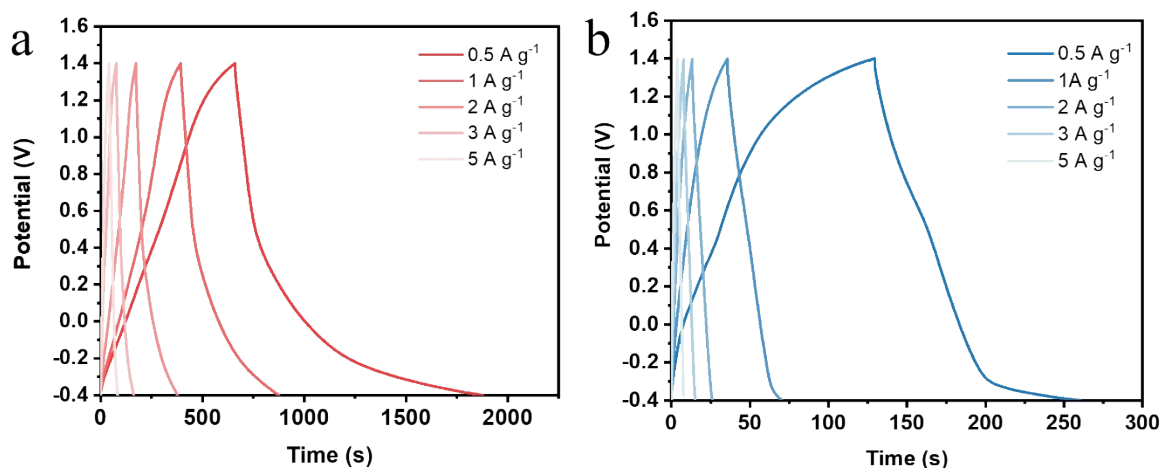
Figure17. GCD curves at different current densities from 0.5 to 5 A g^{-1} base on a three electrode system in 1 M TEABF4 /ACN. (a) Fe-MOF, (b) Cr-MOF.
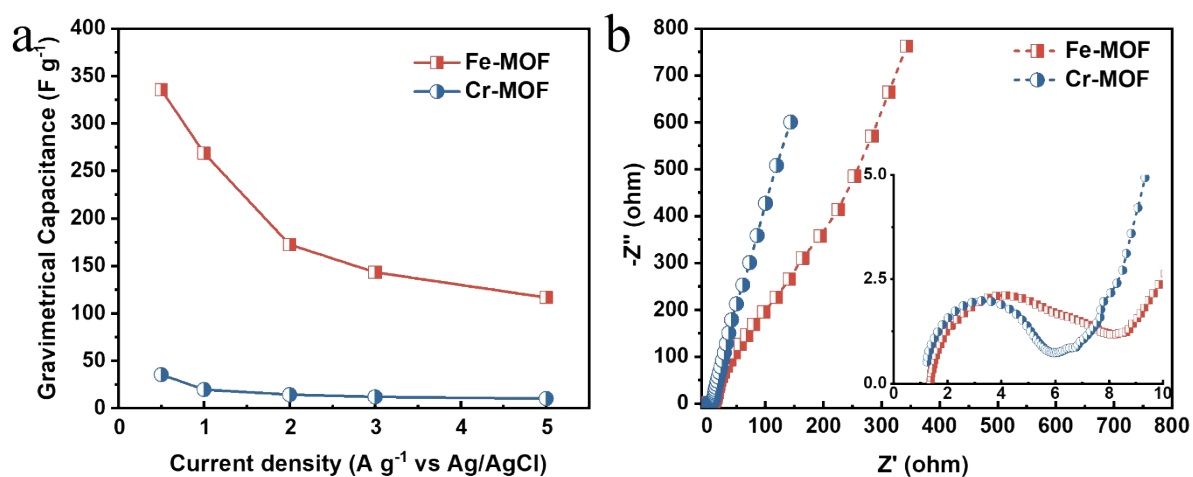
Figure18. Electrochemical tests based on a three electrode system in 1 M TEABF$_4$ /ACN. (a) Rate capability curves of Fe/Cr-MOF electrodes. (b) Nyquist plot of Fe/Cr-MOF electrodes. Inset: high-frequency domain.
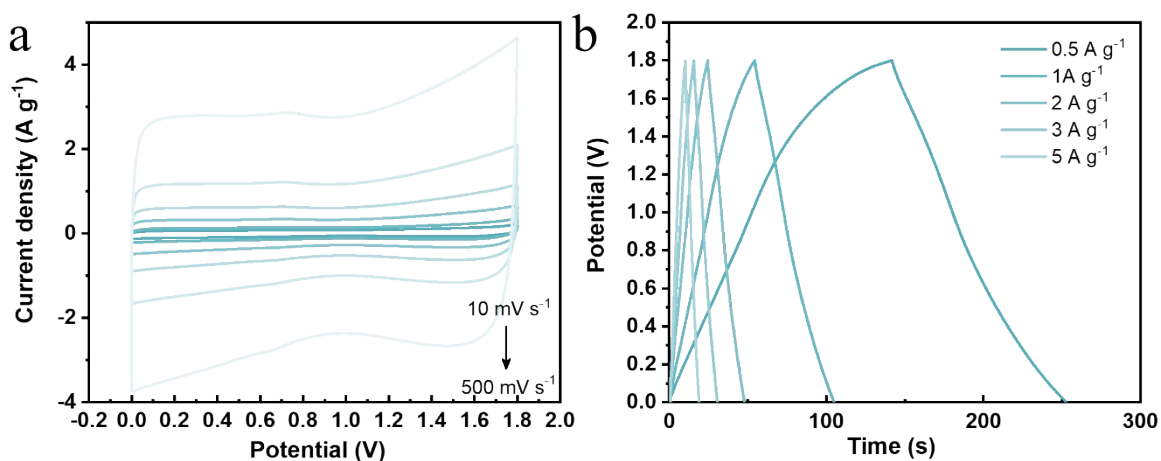
Figure S19. Electrochemical test of Cr-MOF//SC base on a symmetric capacitor in 1 M TEABF$_4$ /ACN. (a) CV curves at different scan rates from 10 to 100 mV s^{-1}. (b) GCD curves at different current densities from 0.5 to 5 A g^{-1}.
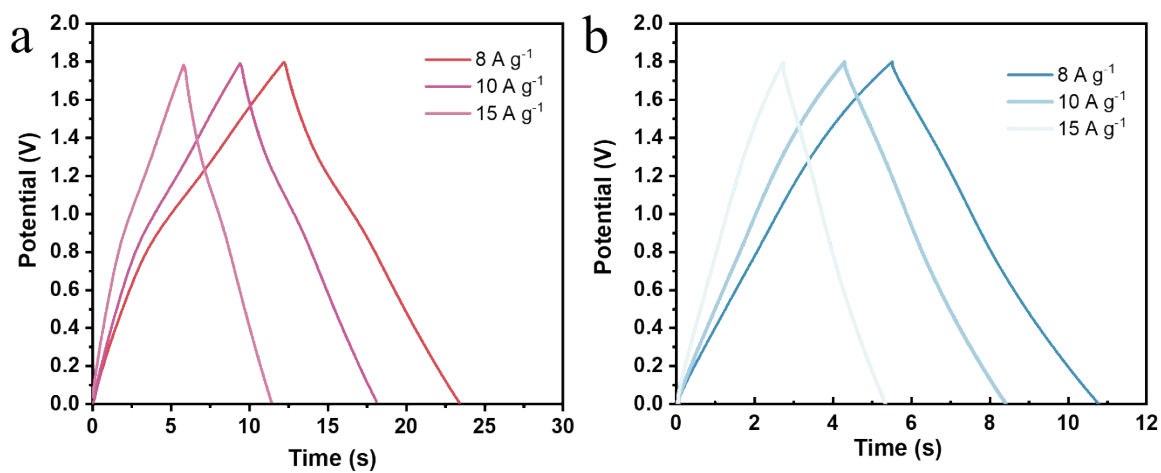
Figure S20. Comparison of GCD curves at high current densities from 8 to 15 A g^{-1} base on a symmetric capacitor. (a) Fe-MOF//SC, (b) Cr-MOF//SC.
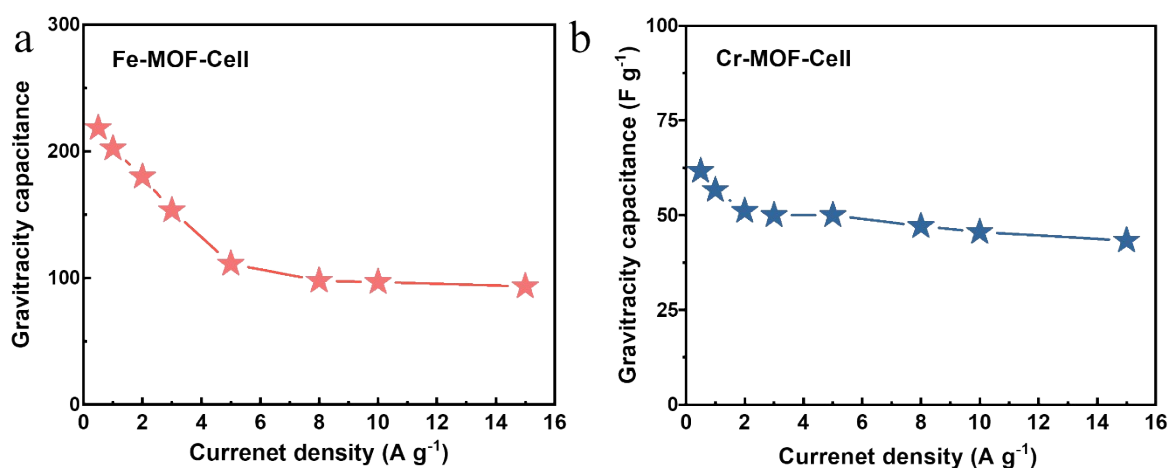
Figure S21. Rate capability curves of cell capacitance based on Fe-MOF//SC (a) and Cr-MOF//SC (b).
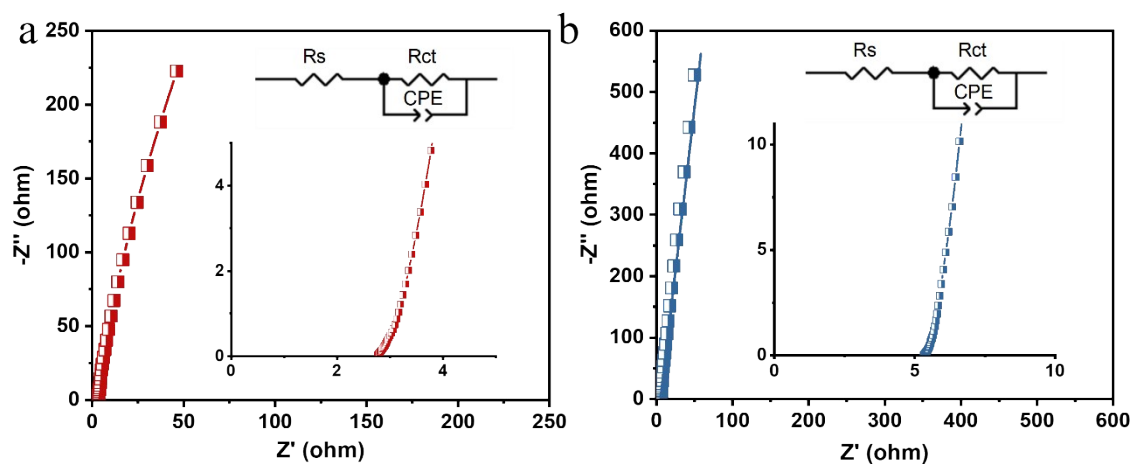
Figure S22. (a) Nyquist plot of Fe-MOF//SC. Inset: high-frequency domain and equivalent circuit plot. (b) Nyquist plot of Cr-MOF//SC. Inset: high-frequency domain and equivalent circuit plot.
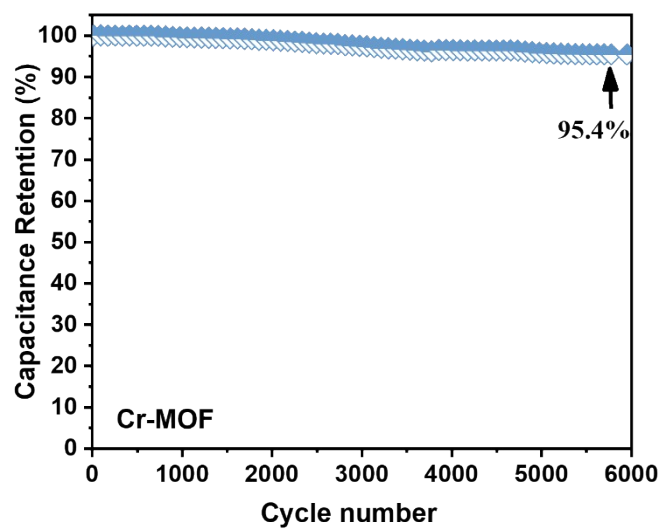
Figure S23. Stability test of the Cr-MOF//SC at a current density of 1 A g^{-1} for 6,000 cycles.
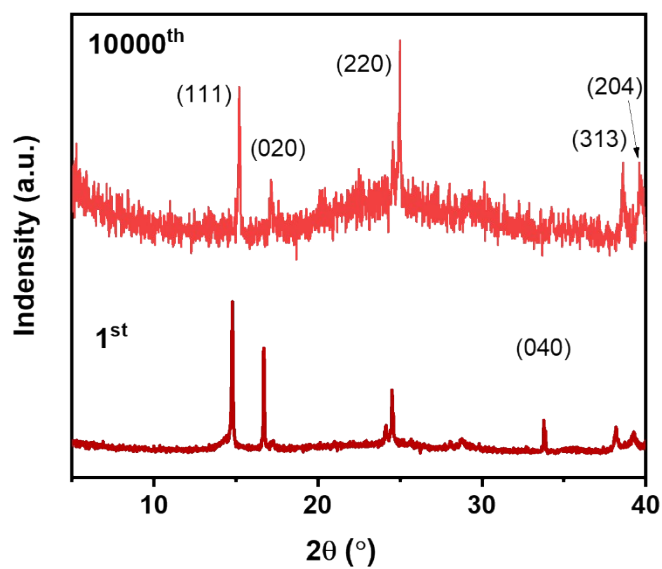
Figure S24. PXRD pattern of Fe-MOF//SC before and after 10000 cycles.
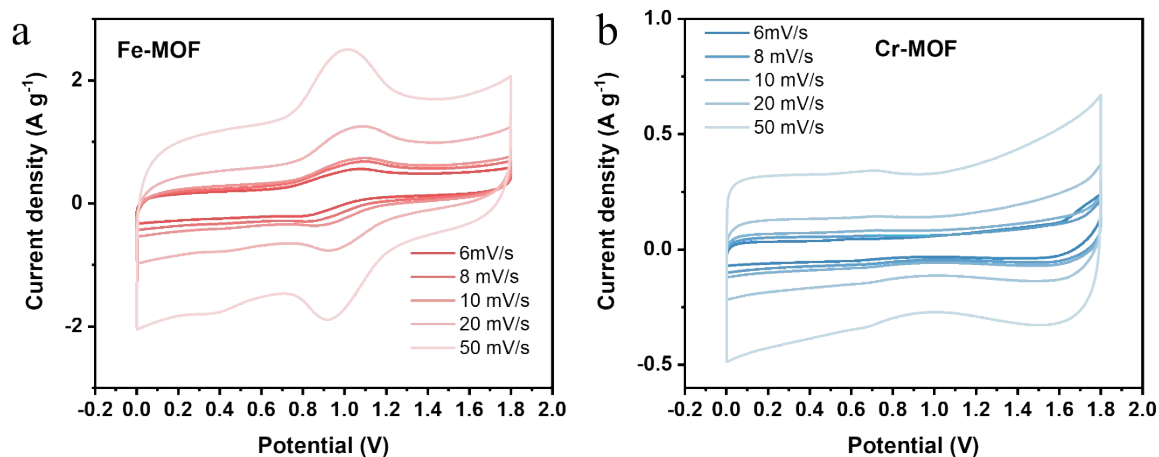
Figure S25. (a-b) CV curves of Fe- and Cr-MOF at different scan rates from 6 to 50 mV s^{-1}.
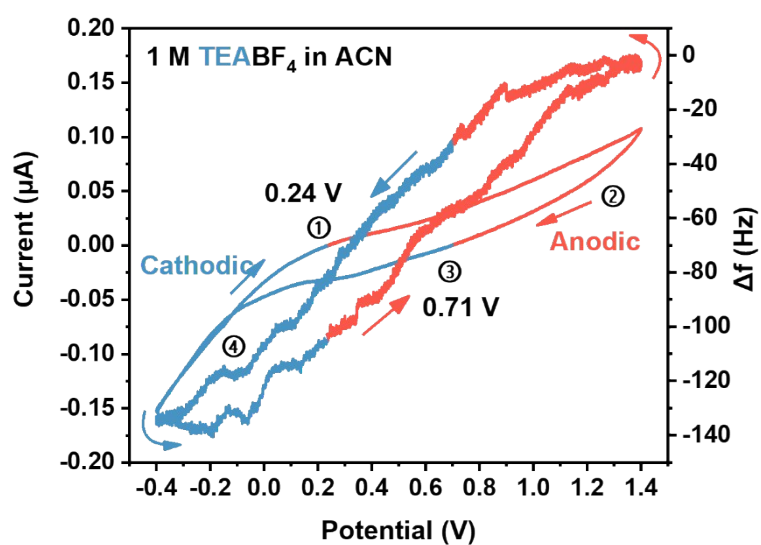
Figure S26. Simultaneously measured QCM frequency responses of the Fe-MOF electrode during a charging-discharging cycle.
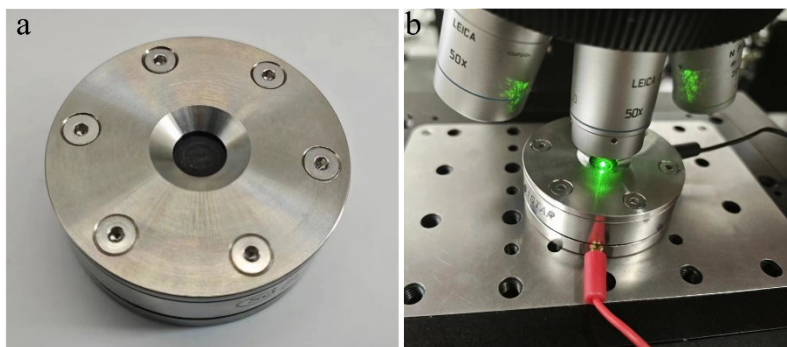
Figure S27. Digital photograph of the symmetric cell for in-situ Raman characterization.
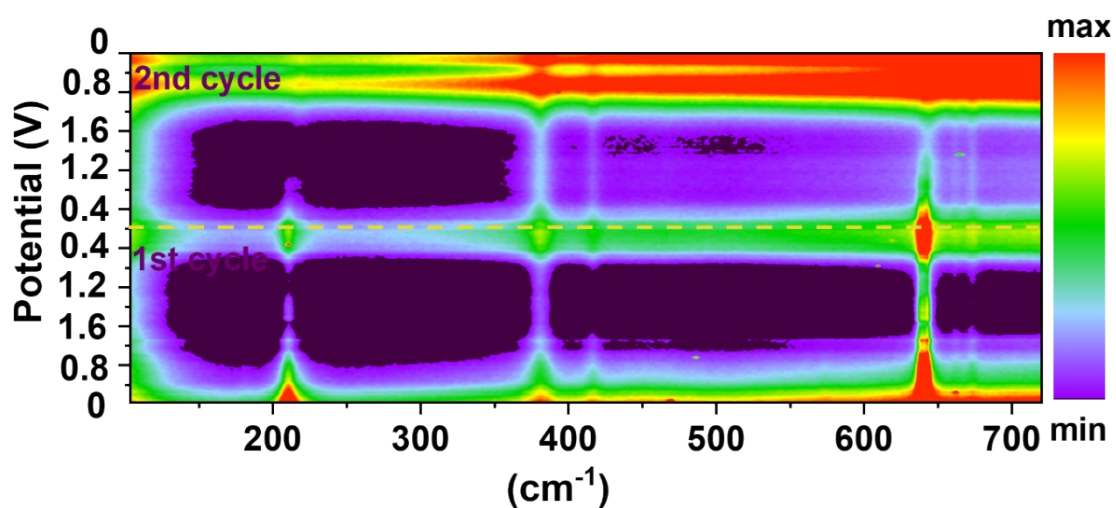
Figure S28. The corresponding contour spectrum plot including the Fe-N stretching-frequency range of 150 to 720 cm^{-1} obtained from two charge/discharge cycles.

Table S1. Comparation crystallographic data of Fe-MOF and Cr-MOF.

	Fe-MOF	Cr-MOF
Empirical formula	$C_8 H_8 Cl_2 Fe N_4$	$C_8 H_8 Cl_2 Cr N_4$
Formula weight	286.93	283.07
Temperature / K	173(2)	/
Crystal system	orthorhombic	orthorhombic
Space group	C c c a	I m m m
a/ Å, b/ Å, c/ Å	10.2066(4),10.5575(4), 10.2661(4)	6.9035(4),6.9771(4), 10.8254(6)
$\alpha/°$, $\beta/°$, $\gamma/°$	90,90,90	90,90,90
Volume / $Å^3$	1106.27(7)	521.428
Z	4	/
ρcalc / mg mm^{-3}	1.723	/
μ / mm^{-1}	15.149	/
F(000)	576	/

Crystal size / mm³	0.200 x 0.180 x 0.160	/
2θ range for data collection	7.419 to 68.076 °	/
Index ranges	-12<=h<=12, -12<=k<=11, -12<=l<=12	/
Reflections collected	3858	/
Independent reflections	513 [R(int) = 0.0627]	/
Data/restraints/parameters	513 / 0 / 36	/
Goodness-of-fit on F²	1.077	/
Final R indexes [I>2σ (I)]	R1 = 0.0449, wR2 = 0.1300	/
Final R indexes [all data]	R1 = 0.0491, wR2 = 0.1369	/
Completeness	1.002	/
CCDC deposition number	2363842	/

Table S2. Comparation of structural data between Fe-MOF and Cr-MOF.

Comparation structural data of Fe-MOF and Cr-MOF				
Intramolecular Bond Distances (Å)				
	$Fe\ C_8\ N_4\ Cl_2\ H_8$		$Cr\ C_8\ N_4\ Cl_2\ H_8$	
M-N	Fe-N	2.224(2)	Cr-N1	2.003(2)
			Cr-N2	2.059(2)
M-Cl	2.405		2.337(1)	
M-M	7.238		6.977(4)	
Bond Angles (deg)				
Cl-M-N	89.7 / 90.3		90	
M-N-C	Fe-N-C1	121.8	Cr-N1-C2	125.6
	Fe-N-C2	122	Cr-N2-C1	124.5
C-N-C	C1-N-C2	116.2(3)	C2-N1-C2	108.8

				C1-N2-C1	72.9
C-C-C		C2-C1-C2	90	C1-C2-C1	90

Table S3. Hyperfine parameters (extracted from the Mössbauer spectra) for the single-crystalline Fe-MOF crystal.

compound	Doublet	Spin state of Fe^{2+} ion	Isomer shift (δ) mm s^{-1}	Quadruple splitting (ΔE_Q) mm s^{-1}	Line width (Γ) mm s^{-1}	Area (R_A) （%）
	A	HS (High Spin)	0.984	3.146	0.402	59.62
Fe-MOF						
	B	HS	1.051	1.758	0.646	40.38

Table S4. Electrical conductivity comparison between Fe-/Cr-MOFs and other literature reported 2D MOFs.

2D conductive-MOF	Method	Type	Conductivity (S cm^{-1})	Ref.
Fe-MOF	**4- Probe**	**Pellet**	**-**	**This work**
Cr-MOF	**4- Probe**	**Pellet**	**9.0×10^{-3}**	**This work**
$Cu_3(HHTP)_2$	2-Probe	Pellet	3.0×10^{-3}	[8]
$Ni_9(HHTP)_4$	2-Probe	Pellet	6.0×10^{-3}	[9]
$Co_9(HHTP)_4$	4-Probe	Pellet	2.7×10^{-6}	[10]
$Cu_2[CuPcO_8]$	2-Probe	Pellet	9.4×10^{-8}	[11]
$Ni_2[NiPcO_8]$	4-Probe	Pellet	7.2×10^{-4}	[12]

$Fe_2[FePcO_8]$	vdP	Pellet	$\sim 1 \times 10^{-5}$	[13]
$Ni_3(HITP)_2$	2-Probe	Pellet	2	[14]
$Co_3(HTTP)_2$	vdP	Pellet	1.4×10^{-3}	[15]
$Fe_3(HTTP)_2$	vdP	Film	3.4×10^{-2}	[16]
$Fe_3(PTC)$	vdP	Pellet	10	[17]

Table S5. Supercapacitive performance comparison of Fe-MOF and Cr-MOF electrodes and other MOF-based electrodes.

Materials	Gravimetric capacitance ($F\,g^{-1}$)	Current density ($A\,g^{-1}$)	Electrolyte	Ref.
Fe-MOF	436.7	0.5	1 M $TEABF_4$/ACN	This work
Cr-MOF	123.5	0.5		
MIL-100(Fe)	30	5 ($mV\,s^{-1}$)	0.1 M Cs_2SO_4	[18]
UiO-66	101.5	0.2	6 M KOH	[19]
Ni-HAB	420	0.5	1 M KOH	[20]
Cu-HAB	215	0.5	1M KOH	[20]

Ni$_3$(HITP)$_2$	111	0.05	1 M TEABF$_4$/ACN	[21]
Cu$_3$(THQ)$_2$-BPY	66.1	10 (mV s^{-1})	1M KOH	[22]
Ni$_3$BHT	195	7 (mV s^{-1})	1 M LiPF$_6$/ACN	[23]
Ti$_3$C$_2$T$_x$ MXene	65	0.5	PVA-H$_2$SO$_4$	[24]
Nitrogen-enriched carbon	245	-	6 M KOH	[25]

Table S6. Areal supercapacitive performance comparison of Fe-MOF and other MOF-based electrodes.

Material	Areal capacitance (mF cm^{-2})	Current density (mA cm^{-2})	Electrolyte	Ref.
Fe-MOF	**269.9**	**0.3**	**1 M TEABF$_4$/ACN**	**This work**
Ni-CAT MOF	15.2	0.2	3 M LiCl	[26]
Ni$_2$[CuPc(NH)$_8$	18.9	0.04	PVA/LiCl	[27]
Fe-HHTP	3.3	-	0.1 M TBAPF$_6$/ACN	[1]
Cu-HHTP	2.4	-	0.1 M TBAPF$_6$/ACN	[1]

Cu-CAT	0.022	0.5(A g^{-1})	PVA/KCl	[8]
MOF@COF-TCNQ	78.36	0.2	0.1 M H$_2$SO$_4$	[28]

Table S7. Equivalent circuit fitting values of Electrochemical impedance spectroscopy (EIS).

Materials	R$_s$(Ω）	R$_{ct}$(Ω）	CPE-T	CPE-P
Fe-MOF	2.89	0.43	0.0066	0.91
Cr-MOF	5.46	0.21	0.0028	0.94

Table S8. Energy density and power density comparison of state-of-art symmetric supercapacitors.

Material	Power density (kW kg^{-1})	Energy density (Wh kg^{-1})	Ref.
Fe-MOF	**0.9**	**98.2**	**This work**
Cr-MOF	**27**	**19.2**	
Cu-DBC	0.1	13.8	[29]
Ni-HAB	0.021	14.8	[20]
nMOF-867	0.62	0.054	[30]
Cu-CAT	0.2	2.6	[8]

GF–CNT@Fe_2O_3	1.4	74.7	[31]
3D Porous Carbon Nanosheet	0.22	24.3	[32]
Ni-MOF	0.8	31.5	[33]
$Ti_3C_2T_x$	0.958	12.8	[34]
Maxwell BCAP3000	5.294	4	[35]
Saft Gen2	3.125	6.0	[35]
Saft Gen3	6.923	6.8	[35]

Section Ⅲ. Reference

1. K. S. Pedersen, P. Perlepe, M. L. Aubrey, D. N. Woodruff, S. E. Reyes-Lillo, A. Reinholdt, L. Voigt, Z. Li, K. Borup, M. Rouzières, D. Samohvalov, F. Wilhelm, A. Rogalev, J. B. Neaton, J. R. Long and R. Clérac, *Nat. Chem.*, 2018, **10**, 1056-1061.
2. M. Wang, M. Ballabio, M. Wang, H.-H. Lin, B. P. Biswal, X. Han, S. Paasch, E. Brunner, P. Liu, M. Chen, M. Bonn, T. Heine, S. Zhou, E. Cánovas, R. Dong and X. Feng, *J. Am. Chem. Soc.*, 2019, **141**, 16810-16816.
3. P. Zhang, M. Wang, Y. Liu, Y. Fu, M. Gao, G. Wang, F. Wang, Z. Wang, G. Chen, S. Yang, Y. Liu, R. Dong, M. Yu, X. Lu and X. Feng, *J. Am. Chem. Soc.*, 2023, **145**, 6247-6256.
4. S. Fleischmann, J. B. Mitchell, R. Wang, C. Zhan, D.-e. Jiang, V. Presser and V. Augustyn, *Chem. Rev.*, 2020, **120**, 6738-6782.
5. J. W. Gittins, K. Ge, C. J. Balhatchet, P.-L. Taberna, P. Simon and A. C. Forse, *J. Am. Chem. Soc.*, 2024, **146**, 12473-12484.
6. Q. Zhang, M. D. Levi, Y. Chai, X. Zhang, D. Xiao, Q. Dou, P. Ma, H. Ji and X. Yan, *Small Methods*, 2019, **3**, 1900246.
7. J. Liu, Y. Liu, N. Liu, Y. Han, X. Zhang, H. Huang, Y. Lifshitz, S.-T. Lee, J. Zhong and Z. Kang, *Science*, 2015, **347**, 970-974.

8. W.-H. Li, K. Ding, H.-R. Tian, M.-S. Yao, B. Nath, W.-H. Deng, Y. Wang and G. Xu, *Adv. Funct. Mater.*, 2017, **27**, 1702067.
9. E. M. Miner, L. Wang and M. Dincă, *Chem. Sci.*, 2018, **9**, 6286-6291.
10. M. Ko, A. Aykanat, M. K. Smith and K. A. Mirica, *Sensors*, 2017, **17**.
11. H. Nagatomi, N. Yanai, T. Yamada, K. Shiraishi and N. Kimizuka, *Chem. Eur. J.*, 2018, **24**, 1806-1810.
12. Z. Meng, A. Aykanat and K. A. Mirica, *J. Am. Chem. Soc.*, 2019, **141**, 2046-2053.
13. C. Yang, R. Dong, M. Wang, P. S. Petkov, Z. Zhang, M. Wang, P. Han, M. Ballabio, S. A. Bräuninger, Z. Liao, J. Zhang, F. Schwotzer, E. Zschech, H.-H. Klauss, E. Cánovas, S. Kaskel, M. Bonn, S. Zhou, T. Heine and X. Feng, *Nat. Commun.*, 2019, **10**, 3260.
14. D. Sheberla, L. Sun, M. A. Blood-Forsythe, S. Er, C. R. Wade, C. K. Brozek, A. Aspuru-Guzik and M. Dincă, *J. Am. Chem. Soc.*, 2014, **136**, 8859-8862.
15. A. J. Clough, J. M. Skelton, C. A. Downes, A. A. de la Rosa, J. W. Yoo, A. Walsh, B. C. Melot and S. C. Marinescu, *J. Am. Chem. Soc.*, 2017, **139**, 10863-10867.
16. R. Dong, P. Han, H. Arora, M. Ballabio, M. Karakus, Z. Zhang, C. Shekhar, P. Adler, P. S. Petkov, A. Erbe, S. C. B. Mannsfeld, C. Felser, T. Heine, M. Bonn, X. Feng and E. Cánovas, *Nat. Mater.*, 2018, **17**, 1027-1032.
17. R. Dong, Z. Zhang, D. C. Tranca, S. Zhou, M. Wang, P. Adler, Z. Liao, F. Liu, Y. Sun, W. Shi, Z. Zhang, E. Zschech, S. C. B. Mannsfeld, C. Felser and X. Feng, *Nat. Commun.*, 2018, **9**, 2637.
18. N. Campagnol, R. Romero-Vara, W. Deleu, L. Stappers, K. Binnemans, D. E. De Vos and J. Fransaer, *ChemElectroChem*, 2014, **1**, 1182-1188.
19. W. Gao, D. Chen, H. Quan, R. Zou, W. Wang, X. Luo and L. Guo, *ACS Sustain. Chem. Eng.*, 2017, **5**, 4144-4153.
20. D. Feng, T. Lei, M. R. Lukatskaya, J. Park, Z. Huang, M. Lee, L. Shaw, S. Chen, A. A. Yakovenko, A. Kulkarni, J. Xiao, K. Fredrickson, J. B. Tok, X. Zou, Y. Cui and Z. Bao, *Nat. Energy*, 2018, **3**, 30-36.
21. S. Bi, H. Banda, M. Chen, L. Niu, M. Chen, T. Wu, J. Wang, R. Wang, J. Feng, T. Chen, M. Dincă, A. A. Kornyshev and G. Feng, *Nat. Mater.*, 2020, **19**, 552-558.
22. J. Y. Choi, J. Flood, M. Stodolka, H. T. B. Pham and J. Park, *ACS Nano*, 2022, **16**, 3145-3151.
23. S.-J. Shin, J. W. Gittins, C. J. Balhatchet, A. Walsh and A. C. Forse, *Adv. Funct. Mater.*, 2023, **n/a**, 2308497.
24. D. Jiang, J. Zhang, S. Qin, Z. Wang, K. A. S. Usman, D. Hegh, J. Liu, W. Lei and J. M. Razal, *ACS Nano*, 2021, **15**, 5000-5010.
25. J. Li, Z. Xia, X. Wang, C. Feng, Q. Zhang, X. a. Chen, Y. Yang, S. Wang and H. Jin, *Adv. Mater.*, 2024, **36**, 2310422.
26. H. Wu, W. Zhang, S. Kandambeth, O. Shekhah, M. Eddaoudi and H. N. Alshareef, *Adv. Energy Mater.*, 2019, **9**, 1900482.
27. M. Wang, H. Shi, P. Zhang, Z. Liao, M. Wang, H. Zhong, F. Schwotzer, A. S. Nia, E. Zschech, S. Zhou, S. Kaskel, R. Dong and X. Feng, *Adv. Funct. Mater.*, 2020, **30**, 2002664.
28. H. Peng, S. Huang, D. Tranca, F. Richard, W. Baaziz, X. Zhuang, P. Samorì and A. Ciesielski, *ACS Nano*, 2021, **15**, 18580-18589.
29. J. Liu, Y. Zhou, Z. Xie, Y. Li, Y. Liu, J. Sun, Y. Ma, O. Terasaki and L. Chen, *Angew. Chem. Int. Ed.*, 2020, **59**, 1081-1086.
30. K. M. Choi, H. M. Jeong, J. H. Park, Y.-B. Zhang, J. K. Kang and O. M. Yaghi, *ACS Nano*, 2014, **8**, 7451-7457.
31. C. Guan, J. Liu, Y. Wang, L. Mao, Z. Fan, Z. Shen, H. Zhang and J. Wang, *ACS Nano*, 2015, **9**, 5198-5207.

32. X.-h. Zhang, X.-y. Gan, B.-s. Liu, X.-y. Yan and X.-x. Zhao, *New Carbon Mater.*, 2021, **36**, 594-605.
33. S. Gao, Y. Sui, F. Wei, J. Qi, Q. Meng and Y. He, *J. Mater. Sci.*, 2018, **53**, 6807-6818.
34. S. Venkateshalu and A. N. Grace, *Electrochim. Acta*, 2020, **341**, 136035.
35. A. Burke, *J. Power Sources*, 2000, **91**, 37-50.